Spin-Unrestricted and Spinor Nonradiative Relaxation Dynamics in Functionalized Semiconductors

Talgat Inerbaev,[*,1,2] **Aaron Forde,**[3] **Stephanie J. Jensen,**[4] **and Dmitri Kilin**[5]

[1]Sobolev Institute of Geology and Mineralogy SB RAS, Novosibirsk, 630090

[2]L. N. Gumilyov Eurasian National University, Astana, Kazakhstan, 010008

[3]Department of Materials Science and Nanotechnology, North Dakota State University, Fargo, North Dakota 58102, United States

[4]Department of Physics, Wake Forest University, Winston-Salem, North Carolina 27109, United States

[5]Department of Chemistry and Biochemistry, North Dakota State University, Fargo, North Dakota 58108, United States

[*]E-mail: Talgat.inerbaev@gmail.com

In this paper, we give a review of our recent successes in the further development of the density matrix theory to describe the nonequilibrium charge dynamics in semiconductor systems with open electron shells. They are considered two approaches to describe these systems. In the first, systems with a negligibly small spin-orbit coupling are examined, where the description of the electron dynamics is reduced to separate consideration of electrons with different spin directions. If the spin-orbit interaction cannot be neglected, the charge dynamics can be described in the basis of two-component spinors, where spin-flip transitions are allowed. Examples of practical use of the theory in specific cases are given for both methods of description.

Introduction

This chapter is a review of our recent advances in the further development of the theory for describing nonequilibrium electron dynamics in semiconductors, including both bulk and nanoscale systems. Over the past three years, we have made significant progress in the development of the reduced density matrix method for describing these processes. The result of the efforts is the possibility of describing non-radiative relaxation taking into account electron spin polarization, the spin-orbit interaction, as well as the consideration of periodic systems with indirect optical transitions.

The ultimate motivation for this work is the need to develop low-cost, high-performance materials for solar energy harvesting and optoelectronic applications (*1–4*). For a theoretical

© 2019 American Chemical Society

Kilin et al.; Computational Photocatalysis: Modeling of Photophysics and Photochemistry at Interfaces
ACS Symposium Series; American Chemical Society: Washington, DC, 2019.

description of the processes occurring in materials used for such purposes, it is necessary to take into account the interaction of the electrons and ions, including those in which nonradiative relaxation of electronic excitations occurs. This kind of description goes beyond the adiabatic approximation, and in this case, special modeling methods should be applied. It is the further development of one of these theoretical approaches, namely the method of the reduced density matrix, discussed in this paper.

Irradiation of a semiconductor with photon energy greater than its bandgap leads to light absorption and formation of a highly delocalized and energetic exciton. In the process of relaxation, the exciton loses energy through interaction with the ionic subsystem, which is also accompanied by the localization of the electron and hole. The lowest energy states for the electron and hole are at the surface sites, so charge carriers tend to migrate in random electron hopping events until they reach the surface.

The interaction of the semiconductor solar energy converter with electromagnetic radiation occurs in a few steps. The first is the light capture - absorption of the sunlight, resulting in an electron-hole pair excitation. The second is the electron transfer - sunlight-produced electron and hole diffuse to the surface sites, separated in space (5). This process is accompanied by electron and hole relaxation toward the conduction band (CB) minimum and valence band (VB) maximum, respectively, and they are key in solar cells (6–8). During this step, electronic excitation energy is partially lost to thermal energy of lattice vibrations via electron−phonon interactions. In photocatalysis, there is one more important step in fuel synthesis - the efficient making and breaking of the chemical bonds using the harvested electron-hole pairs.

There are a huge range of possible semiconductor materials, and among this set, various limitations may reduce the number of materials for study. Requirements include factors such as abundance/cost, toxicity, stability, match of band-edge potentials to desired electron transfer reactions, and match of bandgap to visible photon energy (9–12). In a number of materials containing heavy elements, spin-orbit coupling (SOC) begins to play a significant role (13–16). To assess the role of the SOC, suite of codes for nonadiabatic dynamics has been developed for two-component spinor orbitals (17).

Further, this chapter is organized as follows. First, we describe the reduced density matrix method before our expansion to the cases mentioned above. Then, its extensions will be considered for the cases of (i) spin-polarized states and (ii) of electronic dynamics taking into account SOC. Both cases are accompanied by examples of use for describing specific systems.

Reduced Density Matrix Method

Due to the fundamental role of radiationless processes in chemical reactivity, there is abundant literature devoted to extracting nonadiabatic coupling (NAC) from computer simulations. Theoretical approaches utilized for this purpose fall into two general categories: trajectory-based methods and techniques based on direct propagation of the reduced density operator. The latter set of methods includes the mean-field Ehrenfest (18), surface-hopping (19–21), semiclassical initial value representation (22), linearization (23, 24), and classical mapping (25, 26) approaches. The former techniques are based on evolution of the reduced density matrix (RDM) and consider Redfield equations (27) and the noninteracting blip approximation (28), which serves as a time-dependent generalization of Förster theory (29).

Spin-unrestricted electronic structure (30) was found useful in describing materials with spin polarization. An approximate treatment can be pursued in the basis of spin-collinear density

functional theory (*31, 32*). Most transition-metal compounds exhibit open shell non-singlet configurations, necessitating special treatment of electrons with α/β spin projections. By separate treatment of electronic states with the α/β spin components one is able to describe a broader range of materials, identify new channels of relaxation and charge transfer, and provide knowledge for rational design of new materials in solar energy harvesting and information storage. For this methodology, named spin-resolved electron dynamics, spin-polarized DFT is used as the basis to implement nonadiabatic charge relaxation dynamics (*33*). When considering the dynamics of spin-polarized electronic states, neglecting the spin-orbit interaction, it is natural to treat states with different spin projections as an independent. Therefore, the theoretical description, in this case, differs from the consideration of spin-restricted systems by the introduction of an additional spin index in the formulas. Below we present a brief description of the reduced density matrix method suitable for describing systems with both closed and open electron shells.

Spin-Unrestricted Theory of Nonadiabatic Electron Dynamics with RDM Method

The basic idea in microscopic theory of nonadiabatic charge dynamics is a decomposition of a total system into a subsystem of interest and bath parts. In our case, the former one corresponds to electronic, while the latter one is an ionic part. Complete time-dependent Hamiltonian of a problem under consideration is written as a sum of electronic Hamiltonian $\hat{H}^{el}$, an ionic Hamiltonian $\hat{H}^{ion}$, and their interaction $\hat{H}^{int}$

$$\hat{H}(\boldsymbol{R}, \boldsymbol{r}, t) = \hat{H}^{el}(\boldsymbol{R}(t), \boldsymbol{r}) + \hat{H}^{ion}(\boldsymbol{R}(t)) + \hat{H}^{int}(\boldsymbol{R}(t), \boldsymbol{r}) \qquad (1)$$

where $\boldsymbol{R}$ *(t)* represents the nuclear coordinates evolving along a classical path, $\boldsymbol{r}$ is the electronic coordinates, and *t* is time. The system under consideration is isolated. In this case, one can consider the electronic subsystem as open and immerse in an ionic thermostat. The traditional quantum mechanical method for describing such systems is the density operator method.

The density operator is a powerful theoretical tool combining quantum mechanics and thermodynamics. It allows describing an open system interacting with the environment: solvent, substrate, lattice vibrations, or quantized radiation (*34–39*). The density operator provides a quantum picture of energy dissipation, photoemission, and dephasing. In our particular case the operator obtained after averaging over ionic degrees of freedom (DOF) is a reduced density operator (RDO) (*18*). Dependence of $\hat{H}^{el}$ on the ionic DOF emphasizes the nonadiabatic character of charge dynamics in the system under investigation.

The time-dependent density operator is formally defined as the outer product of the wavefunction and its conjugate (σ is a spin index)

$$\hat{\rho}_\sigma(t) = |\psi_\sigma(t)\rangle\langle\psi_\sigma(t)| = \sum_{ij} c_{i,\sigma}(t) c_{j,\sigma}^*(t) |i_\sigma\rangle\langle j_\sigma| = \sum_{ij} \rho_{ij,\sigma}(t) |i_\sigma\rangle\langle j_\sigma| \quad (2)$$

where we expanded the wavefunction with respect to the eigenstates of some Hermitian operator

$$\psi_\sigma(t) = \sum_i c_{i,\sigma}(t) |i_\sigma\rangle \quad (3)$$

.

The density operator follows the von-Neumann equation of motion (EOM)

$$\frac{\partial \widehat{\rho}_\sigma}{\partial t} = -\frac{i}{\hbar}\left[\widehat{H}, \widehat{\rho}_\sigma(t)\right], (4)$$

which is considered further in the framework of perturbation theory, where the $\widehat{H}^{int}$ is the small parameter. In addition, we use Born and Markov approximations (*18*). Born approximation corresponds to the weak electron-ion coupling, so that the back-action of the system onto the bath can be neglected. This approximation allows us to consider the ionic subsystem as a thermodynamically equilibrium one and justifies averaging over ionic DOF. Within the Markov approximation it is assumed that system correlation time is short.

We focus on EOM for electronic DOF and take into account the influence of thermalized ionic motion in an approximate fashion, similar to the Redfield approach (*27*). Formally, one has to solve a problem of time-dependent evolution in terms of density operator $\widehat{\rho}$. Total density operator can be factorized on electronic $\widehat{\rho}^{\,el}$ and ionic $\widehat{\rho}^{\,ion}$ components and that the ionic density operator obeys thermal equilibrium distribution. A natural simplification of the considered operator is its averaging over ionic degrees of freedom, which is calculated as $\widehat{\rho}^{el} = \mathrm{Tr}_{ion}\left(\widehat{\rho}^{tot}\right)$. The obtained operator $\widehat{\rho}^{el}$ includes an additional term containing information about the effect of lattice vibrations on the electronic structure of the object under study. This term, commonly referred to as the Redfield term (*40*), can be obtained as second-order perturbation with respect to the electron-phonon interaction Hamiltonian as described below.

According to this approach, the following equation describes the time evolution of the operator $\widehat{\rho}^{el}$

$$\frac{\partial \widehat{\rho}^{el}}{\partial t} = -\frac{i}{\hbar}\left[\widehat{H}^{el}, \widehat{\rho}^{el}(t)\right] -$$
$$\frac{1}{\hbar^2}\int_0^t d\tau \, Tr_{ion}\left\{\left[\widehat{H}^{int}(0), \left[\widehat{H}^{int}(\tau), \widehat{\rho}^{el}(t)\widehat{\rho}^{ion}\right]\right]\right\} (5)$$

The right side of Eq. 5 contains two terms, the first of which describes reversible dynamics. In contrast, the second term is very specific. It uses Hamiltonian of interaction of electrons and lattice vibrations $\widehat{H}^{int}$. This Hamiltonian is small compared to $\widehat{H}^{el}$ and serves as a small parameter for perturbation theory. The consideration is carried out in the second order of the perturbation theory, since the first-order correction is zero. The integration limit runs from the instant the interaction was switched on until the time we focus on. The symbol Tr_{ion} corresponds to an average over states of the ionic subsystem, in thermal state, which is characterized by the ion density operator $\widehat{\rho}^{ion}$. The Hamiltonian of interaction $\widehat{H}^{int}$ enters there twice: at the initial instant of time $t=0$ and at the delayed instant of time $t=\tau$ that corresponds to two elementary events of interaction, separated by the time interval τ. During the interval between these events, there appears an accumulation of phase described by the first elastic term in Eq. 5, corresponding to time evolution of non-interacting ionic and electronic subsystems. The interaction Hamiltonian is often factorized as a bilinear product of relevant operators affecting the electronic subsystem and ionic lattice subsystem.

In case the wave function is decomposed in a chosen basis $\{|i\rangle\}$ (Eq. 3), the density operator (2) converts into density matrix $\rho_{ij} = \langle i|\widehat{\rho}|j\rangle$ for electronic DOF (*27, 34–39*). RDM obeys Redfield EOM

$$\frac{\partial \widehat{\rho}_{ij}^{el}}{\partial t} = -\frac{i}{\hbar}\sum_k \left[\widehat{H}_{ik}^{el}, \widehat{\rho}_{kj}^{el}\right] + \sum_{kl} R_{ijkl}\widehat{\rho}_{kl}^{el} \quad (6)$$

The Redfield tensor controls dissipative dynamics of density matrix

$$\left(\frac{\partial \hat{\rho}_{ij}^{el}}{\partial t}\right)_{diss} = \sum_{kl} R_{ijkl} \hat{\rho}_{kl}^{el} \quad (7)$$

Its elements are expressed in terms of partial rates $\Gamma^{\pm}$

$$R_{ijkl} = \Gamma_{ljik}^{+} - \delta_{jl} \sum_m \Gamma_{immk}^{+} + \Gamma_{ljik}^{-} - \delta_{ik} \sum_m \Gamma_{jmml}^{-} \quad (8)$$

which in turn are calculated in terms of autocorrelation functions of the interaction Hamiltonian

$$\Gamma_{ljik}^{+} = \int_0^t d\tau M_{lijk}(\tau) \exp(-i\omega_{ik}\tau) \quad (9)$$

$$\Gamma_{ljik}^{-} = \int_0^t d\tau M_{lijk}(-\tau) \exp(-i\omega_{ik}\tau) \quad (10)$$

The phase increment factors $\exp(-i\omega_{ik}\tau)$ appear from the time evolution of the electronic DOF and use energy difference $\hbar\omega_{ij} = \varepsilon_j - \varepsilon_i$. Information on the interaction of the electron and lattice subsystems is now contained in the autocorrelation function of the $\hat{H}^{int}$

$$M_{lijk}(\tau) = M'_{lijk}(\tau, 0) = Tr_{ion}\left\{H_{lj}^{int}(\tau)H_{ik}^{int}(0)\right\} \quad (11)$$

with an assumption $M'(\tau, 0) = M'(\tau + \tau', \tau')$. Here we define

$$\hat{H}_{lj}^{int}(\tau) = \langle l|e^{-i\hat{H}^{ion}\tau}\hat{H}^{int}(0)e^{i\hat{H}^{ion}\tau}|j\rangle \quad (12)$$

Note that approximations we have committed lead to the time-independent coefficients R_{ijkl} for system of linear differential Eq. (7).

In order to apply this theory in practice, it is necessary to obtain an explicit expression for the Hamiltonian $\hat{H}_{lj}^{int}$. For this purpose, following approach presented in Ref. (*41*) we consider the time evolution of the system under consideration using the time-dependent Schrödinger equation

$$i\hbar \frac{\partial \Phi(R,r,t)}{\partial t} = \hat{H}(\boldsymbol{R},\boldsymbol{r})\Phi(\boldsymbol{R},\boldsymbol{r},t) \quad (13)$$

where $\Phi(\boldsymbol{R},\boldsymbol{r},t)$ is the wavefunction of the whole system. We expand this wave function in terms of the orthonormal adiabatic wave functions

$$\Phi(\boldsymbol{R},\boldsymbol{r},t) = \sum_n c_n(t)\Psi_n(\boldsymbol{R},\boldsymbol{r}) = \sum_n c_n(t)|n\rangle \quad (14)$$

where $c_n(t)$ are complex-valued expansion coefficients.

If we substitute expansion Eq.(14) into the time-dependent Schrödinger equation (13) and perform some algebraic transformations, we get

$$i\hbar \frac{\partial c_m(t)}{\partial t} = \sum_n c_n(t)\left(H_{nm} + H_{nm}^{int}\right) \quad (15)$$

Here, $H_{nm} = \langle n|\hat{H}^{el}|m\rangle$ are the matrix elements of the electronic Hamiltonian, and

$$H_{nm}^{int} = -i\hbar V_{nm}, \quad (16)$$

are the matrix elements of the $\widehat{H}^{int}$. $V_{nm} = \left\langle n \left| \frac{\partial}{\partial t} \right| m \right\rangle$ are the scalar non-adiabatic couplings (NACs). From the obtained result, it is evident that $-i\hbar V_{nm}$ are the matrix elements of the Hamiltonian of the interaction between the electron and ion subsystems.

The NACs calculation procedure can be efficiently implemented on the basis of "on-the-fly" adiabatic *ab initio* molecular dynamics (42–44). There, atomic subsystem is represented by a set of subsequent coordinates and momenta along the molecular dynamic trajectories. Practically, the NACs are computed using the finite difference scheme (41):

$$V_{mn}(t) = \frac{\langle m(t)|n(t+\Delta t)\rangle - \langle m(t+\Delta t)|n(t)\rangle}{2\Delta t} \quad (17)$$

In numerical form, based on the derivative of the Hamiltonian, the autocorrelator Eq. (11) is composed of the terms including products of matrix elements V_{kl}^{α} and momentum-momentum correlation function

$$M_{klmn}^{\alpha\beta}(\tau) = \sum_{t,\alpha,\beta} V_{kl}^{\alpha}(t) V_{mn}^{\beta}(t+\tau) \quad (18)$$

To summarize, the system of differential Eq. (7) is numerically solved as follows. At a given temperature, calculations are performed using the molecular dynamics method of atomic trajectories. From the obtained data, including atomic coordinates and pulses, as well as wave functions for each configuration, the components of the Redfield tensor (8) are calculated using relations (7-10), (18).

Practically our modeling is based on the fictitious one electron Kohn-Sham (KS) (45, 46) equation:

$$\left(\frac{-\bar{\hbar}^2}{2m} \nabla^2 + v[\boldsymbol{r}, \boldsymbol{R}, \rho_\sigma(\vec{r})] \right) \varphi_{\sigma,i}^{KS}(\boldsymbol{r}, \boldsymbol{R}) = \varepsilon_{\sigma,i}\{\boldsymbol{R}\} \varphi_{\sigma,i}^{KS}(\boldsymbol{r}, \boldsymbol{R}),$$
(19)

In Eq. (19), one finds the set of one-electron orbitals $\varphi_{\sigma,i}^{KS}(\boldsymbol{r}, \boldsymbol{R})$ with orbital energy levels $\varepsilon_{\sigma,i}\{\boldsymbol{R}\}$. The orbitals are combined with orbital occupation functions $\{f_{\sigma,i}\}$, to construct the total density of electrons

$$\rho_\sigma(\boldsymbol{r}) = \sum_i f_{\sigma,i} \rho_{\sigma,i}^{KS}(\boldsymbol{r}) . \quad (20)$$

The partial charge density $\rho_i^{KS}(\vec{r})$ of orbital number *i* is

$$\rho_{\sigma,i}^{KS}(\boldsymbol{r}) = \varphi_{\sigma,i}^{KS*}(\boldsymbol{r}) \varphi_{\sigma,i}^{KS}(\boldsymbol{r}). \quad (21)$$

Eqs (19-21) are solved in the iterative, self-consistent manner using VASP (47, 48) software using DFT with PAW (49, 50) pseudopotentials and PBE functional (51).

Observables

Solution of Eq. (7) provides time dependent elements of density matrix $\rho_{\sigma,ij}(t)$. Diagonal elements, $\rho_{\sigma,ii}(t)$ determine time-dependent occupations of KS orbitals. Dynamics of charge density distribution, rate of energy dissipation, and rate of charge transfer can be calculated. Specifically, the nonequilibrium distribution of charge as a function of energy reads

$$n^{neq}(\varepsilon, t) = \sum_i \rho_{\sigma,ii}(t)\delta_\sigma(\varepsilon - \varepsilon_{\sigma,i}). \quad (22)$$

The difference of the non-equilibrium distribution obtained from Eq. (6) and the equilibrium distribution

$$n^{eq}(\varepsilon) = \sum_i \delta(\varepsilon - \varepsilon_{\sigma,i}) \quad (23)$$

provides the comprehensive explanation of electron and hole dynamics as a function of energy and time. The change of population with respect to the equilibrium distribution is then expressed as

$$\Delta n_\sigma(\varepsilon, t) = n^{neq}(\varepsilon, t) - n^{eq}(\varepsilon). \quad (24)$$

This equation describes the dynamics of a population gain when $\Delta n > 0$ and a population loss when $\Delta n < 0$ at energy ε, which corresponds to the electron and the hole parts of an excitation. The expectation energy of a photo-excited electron, can be expressed as follows:

$$<\Delta\varepsilon_\sigma^e>(t) = \sum_i \rho_{\sigma,ii}(t)\varepsilon_\sigma^e \quad (25)$$

$$< E_{e,\sigma} > (t) = \frac{<\Delta\varepsilon_\sigma^e>(t) - <\Delta\varepsilon_\sigma^e>(\infty)}{<\Delta\varepsilon_\sigma^e>(0) - <\Delta\varepsilon_\sigma^e>(\infty)} \quad (26)$$

The expectation values of a photo-excited hole are defined analogously. The partial charge density distributions in the conduction and valence bands as functions of, for example, coordinate z and time t can be obtained from the average of the density operator after integration over x and y, and are given by

$$\Delta n_{CB}^{(\sigma,ab)}(z, t) = \sum_{ij\epsilon CB} (\rho_{\sigma,ij}^{(\sigma,ab)}(t) -$$
$$\rho_{\sigma,ij}^{ref}) \int dxdy \left(\varphi_{\sigma,i}^{KS}(\mathbf{r})^* \varphi_{\sigma,j}^{KS}(\mathbf{r})\right), \Delta n_{CB,}^{\sigma,ab} > 0 \quad (27)$$

$$\Delta n_{VB}^{(\sigma,ab)}(z, t) = \sum_{ij\epsilon VB} \left(\rho_{\sigma,ij}^{ref} -$$
$$\rho_{\sigma,ij}^{(\sigma,ab)}(t)\right) \int dxdy \left(\varphi_{\sigma,i}^{KS}(\mathbf{r})^* \varphi_{\sigma,j}^{KS}(\mathbf{r})\right), \Delta n_{VB,}^{(\sigma,ab)} > 0 \quad (28)$$

where $\varphi_{\sigma,i}(\mathbf{r})$ is the i, j^{th} KS orbital, and the indices i and j belong to the conduction or valence bands. The reference density operator ρ^{ref} describes the system in a steady state before light is turned off at time $t=0$. These densities describe the dynamics of charge rearrangement over time after light is removed and the system eventually decays back to equilibrium. In what follows, we focus on the long-time limit $t > \tau_{coh}$, $\tau_{coh} \approx 10\ fs$, which leads to decoherence and the limit $\rho_{\sigma,ij} \to 0$, for $i \neq j$. These distributions reflect the time evolution of the charge transfer along the z

direction in the system. Combining Eqs. (27) and (28), one obtains the variation of the total density as a function of time and position,

$$\Delta n_{total}^{(\sigma,ab)}(z,t) = \Delta n_{CB}^{(\sigma,ab)} - \Delta n_{VB}^{(\sigma,ab)}. \text{ (29)}$$

Calculated rates of relaxation for electrons and holes are computed as follows:

$$k_e = \{\tau^e\}^{-1} = \left\{\int_0^\infty \langle E_e \rangle(t)dt\right\}^{-1} \text{ (30)}$$

$$k_h = \{\tau^h\}^{-1} = \left\{\int_0^\infty \langle E_h \rangle(t)dt\right\}^{-1} \text{ (31)}$$

where $\langle E_e \rangle(t)$ and $\langle E_h \rangle(t)$ are the energy expectation values of a photo-excited charge carrier defined in Eqs. 25 and 26 and are assuming an exponential fit, which is most applicable in two cases: relaxation between two states and relaxation through states equally spaced in energy. The considered model is expected to exhibit what is called a *trapping state*, when the population occupies one state for a longer time in comparison to the other states involved in the relaxation. The *trap* can be due to an increased energy sub gap to overcome or the transfer of population between two states with low coupling (52). The mechanism of *trapping* is hypothetically related to concepts of the energy gap law and phonon bottleneck: Electronic transitions are most efficient when energies of orbitals are offset by a value $\Delta \varepsilon_{\sigma,i} = \varepsilon_{\sigma,i+1} - \varepsilon_{\sigma,i}$ matching a normal mode frequency $\Delta \varepsilon_{\sigma,i} \approx \hbar \omega_{vib}$. However, in case such energy offset exceeds any of the available vibrational frequencies, $\Delta \varepsilon_{\sigma,i} > \hbar \omega_{vib}$ the transition becomes less probable.

In practice, the analysis of relaxation of electronic excitations has to begin with a consideration of the brightest optical transitions, for which it is necessary to calculate the linear optical absorption spectra of the object under study. Optical properties are analyzed based on the transition dipole moment matrix elements

$$D_{ij} = e \int \psi_i^* \boldsymbol{r} \psi_j d\boldsymbol{r} \text{ (32)}$$

for transitions between the initial state i and final state j. Oscillator strength is expressed as

$$f_{ij} = |D_{ij}|^2 \frac{4\pi m_e v_{ij}}{3\hbar e^2} \text{ (33)}$$

Here, m_e is the mass of an electron, $\hbar$ is Planck's reduced constant, v_{ij} is the resonant frequency, and e is the charge of the electron. The oscillator strength calculates the probability of absorbing light, which is then used as a weight to calculate linear optical absorption.

Example: Charge Dynamics in Doped TiO$_2$

Here we briefly describe the results of the spin-resolved nonadiabatic excited state dynamics applied to study vanadium(IV) substitutionally doped bulk anatase (53). The choice of a model system in which the vanadium atom replaces the titanium atom, in addition to the practical interest of describing a real photocatalyst (54–58), is also due to its methodological convenience. Since vanadium is following titanium in the periodic table, being placed in the titanium oxide host lattice

leads to one unpaired electron in a doublet ground state, which will facilitate the modeling and interpretation of the data obtained.

The results show that a difference in the electronic structure for α and β spin components determines consequences in optical excitations and electronic dynamics pathways experienced by electrons with α and β spin projections. Specifically, the lone occupied V 3d α-orbital increases the range of absorption and defines the rates and pathways of relaxation for both holes and electrons with α-spin projection. Optical excitations involving occupied V 3d α-orbital are responsible for IR-range absorption, followed by nonradiative relaxation. Certain transitions involving orbitals of α-spin component occur in the visible range and induce localization of a negative charge on the V ion for an extended time period. The slower nonradiative relaxation rate of α-excitations is rationally explained as a consequence of difference of electronic structure for α and β spin projections and specific pattern of energy levels contributed by doping. Specifically, excitations involving orbitals with α-projection of spin experience transitions through larger subgaps in the conduction band compared to the ones experienced by similar excitations involving orbitals with β-projection of spin.
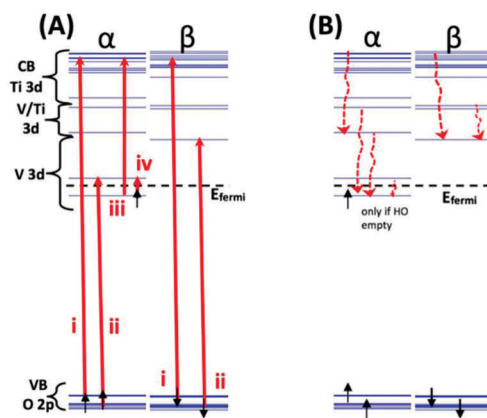

Figure 1. Schematic representation of excitation (A) and relaxation (B) pathways for α and β electron components in vanadium-doped titania. Energies of KS orbitals are represented by bars, electrons occupying such orbitals are symbolized by short up and down arrows for α and β electrons. Character of orbitals is labeled. (A) Possible optical excitations are represented by red straight, solid lines and labeled by roman numerals i–iv, as introduced in the text. (B) Possible nonradiative relaxation pathways are symbolized by dashed wavy arrows. Hole relaxation has been excluded due to triviality. A β-hole will relax quickly to the HO as all VB states are O 2p. Different excitations are marked by lower case roman numerals correlating to eqs 34-36, while relaxation pathway steps are indicated with upper case roman numerals. An α-hole will likely relax quickly through the O 2p states of the VB and stall at the energy jump to the single V state (HO_α). Reproduced with permission from reference (33). Copyright 2016 American Chemical Society.
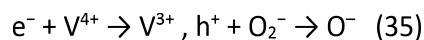
Figure 1 shows the schematic representation of spin unrestricted band structure composed of α and β states for the studied model. As expected, there is only one V 3d orbital occupied by an electron in the ground state configuration, which is in the α set of energy bands. Additionally, four sets of bands are identified, listed from lowest to highest energy: O 2p, V 3d, both hybridized Ti/V and solely Ti 3d intermixed. Energies of orbitals of V/Ti and Ti character are arranged in subsequent order, with V/Ti being "sandwiched" between Ti and V. These are visualized in Figure 2, which shows the density of states along with partial charge density representations for each aforementioned group of energy bands. The details of the brightest optical transitions of each type are presented in detail in Tables 1 and 2 for alpha and beta electrons, respectively.

Four optical transitions types are hypothesized to occur and visualized in Figure 1A, with types iii and iv only allowed for α states; they are listed below along with redox half reactions:
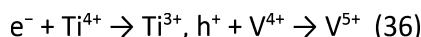
Type i: O 2p to Ti 3d transitions, the only type available in bulk titania,

$$e^- + Ti^{4+} \rightarrow Ti^{3+} , h^+ + O_2^- \rightarrow O^- \quad (34)$$
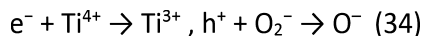
Type ii: O 2p to V 3d transition

$$e^- + V^{4+} \rightarrow V^{3+} , h^+ + O_2^- \rightarrow O^- \quad (35)$$

Type iii: V 3d to Ti 3d transition

$$e^- + Ti^{4+} \rightarrow Ti^{3+}, h^+ + V^{4+} \rightarrow V^{5+} \quad (36)$$

Type iv: V to V 3d intra-atomic transition, which does not change oxidation state. These $d-d$ transitions, are expected to be less intense/sensitive to optical perturbations due to the Laporte selection rule, forbidding transitions, which do not match atomic orbital momentum of $\Delta l = \pm 1$ (59).

Table 1. Computed electronic characteristics for the highest oscillator strength of α-transitions correlating with peaks in the optical absorption spectrum (Figure 3)

α-transitions and relaxation rates						
	donor	*acceptor*	*OS, Arb. units*	*Energy, eV*	*K_e, ps^{-1}*	*K_h, ps^{-1}*
Type *i* α-optical transitions						
A	HO-8	LU+3	14.99	3.10	0.198	0.113
B	HO-7	LU+3	5.69	3.09	0.198	0.110
C	HO-37	LU+6	3.41	4.21	0.243	0.198
D	HO-33	LU+27	3.24	4.42	0.276	0.194
E	HO-26	LU+5	2.91	4.02	0.234	0.186
F	HO-8	LU+2	2.19	2.84	0.347	0.113
Type *ii* α-optical transitions						
G	HO-5	LU+1	0.31	2.34	5.551	0.109
Type *iii* a-optical transitions						
H	HO	LU+2	62.59	0.64	0.347	
I	HO	LU+3	1.38	0.92	0.198	
J	HO	LU+38	0.61	1.76	0.305	
K	HO	LU+6	0.59	1.30	0.243	

Based on the formalism described above, the analysis of non-equilibrium electron relaxation taking into account the spin polarization showed the following. For an α-transition, in general, the localized charges are longer lived compared to those of β. A longer relaxation, and henceforth charge separation, increases the likelihood of the charge catalyzing a reaction or being harvested for light

energy purposes. The longer relaxations for α-holes and electrons are directly related to two things: the hole trapping HO_α-1 state and the larger sub-gap to overcome during electron relaxation.

Table 2. Computed electronic characteristics for the highest oscillator strength of β-transitions correlating with peaks in the optical absorption spectrum (Figure 3)

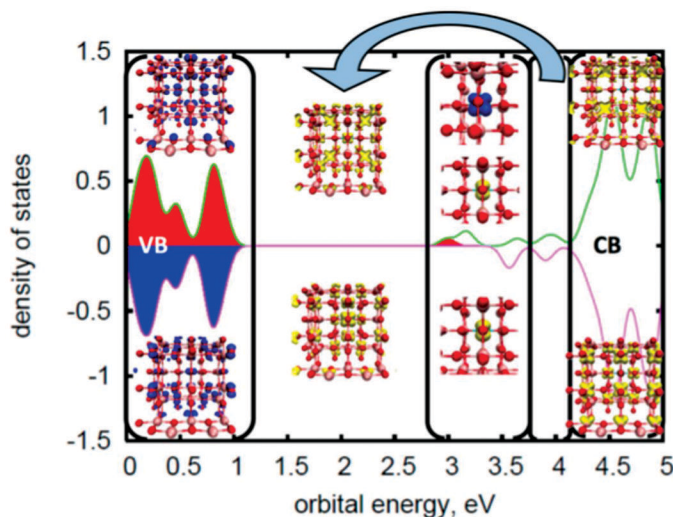|	donor	acceptor	OS, Arb. units	Energy, eV	K_e, ps^{-1}	K_h, ps^{-1}
β-transitions and relaxation rates						
Type *i* β-optical transitions						
A	HO-8	LU+3	14.18	3.09	1.338	2.532
B	HO-8	LU+4	15.14	3.12	0.991	2.532
C	HO-32	LU+28	3.84	4.43	0.482	0.600
D	HO-37	LU+7	3.40	4.25	0.489	0.576
E	HO-21	LU+20	0.75	3.75	0.503	1.922
Type *ii* β-optical transitions						
F	HO-13	LU	0.25	2.80		1.518
G	HO-4	LU+1	0.25	2.74	4.836	10.142

Figure 2. Electronic structure of V(IV) doped anatase in ground state of doublet configuration. Spin-polarized density of states for α (top) and β (bottom) states and corresponding partial charge density isosurface images for certain interval of energy. Filled states and blue (online version) partial charge density isosurfaces represent occupied states whereas no fill and yellow (online version) partial charge density isosurfaces represents unoccupied states. There is a general trend of orbital's character change as orbital energy increases for both α and β orbitals: O 2p to V to V/Ti to Ti. Density of states for states with α-projection of spin, however, has one occupied vanadium state in the vicinity of CB that is expected to alter the energy of electronic states compare to that of β, where all vanadium states are unoccupied. Reproduced with permission from reference (33). Copyright 2016 American Chemical Society.

These indicated conflicting properties for the system as a whole. While β-transitions show very fast relaxation, which could correlate to vanadium being coined as a "recombination center" in an experimental-based article (58), α-transitions show promising properties as a catalytic material. One problem with the conflicting results is the α-transitions that show the longest-lifetime localized negative charge, types i and ii, directly compete for absorption with β types i and ii transitions. Therefore, it would be very difficult to separate the α- and β-transitions without using polarized light or magnetic moments in experiment.
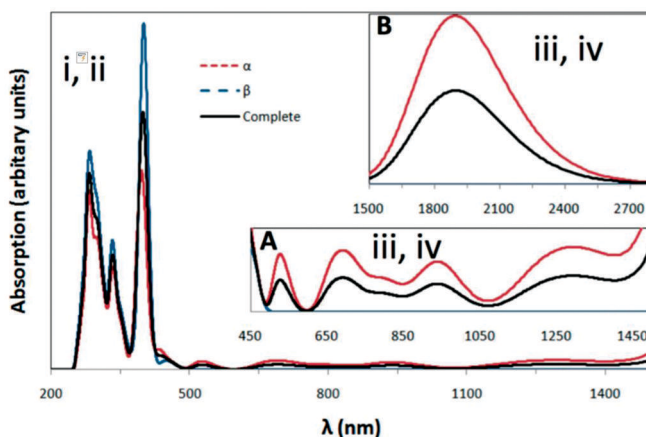

Figure 3. Absorption spectrum for the vanadium (IV) doped anatase model along with transition types for each set of peaks. The peaks attributed to TiO_2 are in the range of 200−500 nm and involve both α- and β-transitions. It is predicted the higher energy peaks are the result of transitions of types i and ii due to larger transition energy and both α- and β-peaks occurring at equal energy and similar amplitude. Additionally, low energy absorption peaks attributed to α electrons in the range of 500−1500 nm are shown in inset A. The largest peak of the system, at about 1900 nm is in inset B and also due to α electrons. All the peaks greater than 500 nm are due to the lone d electron of V (IV) being excited from HO_α and, henceforth, must be transition type iii or iv. Reproduced with permission from reference (33). Copyright 2016 American Chemical Society.

Another property to note is the fact that vanadium can act as either an n- or p-type dopant, where it takes on a negative charge for types i and ii transitions and a positive for type iii transitions. As β-transitions are all n-type for the dopant V, however, short-lived charge, there is no competing processes for this interesting property. The transition where V is a p-type dopant is solely due to an α-transition and the energy difference compared to that of types i and ii transitions is rather significant. It would allow an experiment to exist, where negative charge on vanadium is created by exciting in the 200−450 nm wavelength range and a positive charge for the 700+ nm wavelengths, thus enabling control of charge transfer direction by tuning the wavelength of incident light.

While no surface is available for charge transfer to occur in this specific model, it is predicted that a vanadium (IV) dopant in anatase at or near a surface would embody similar properties mentioned above. Specifically, for α-transitions, a photo-electrochemical cell ideally could harvest the charge (negative for types i and ii transitions, positive for type iii) for use in reducing water into hydrogen and water or other catalytic processes. Additionally, any impurities in the crystal, which cause vanadium lose an electron or gain an electron would alter the results. Losing an electron would cause the loss of the lone V 3d electron and theoretically the $HO_\alpha - 1$ would no longer be a trapping state.

Spinor Dynamics

The above approach describes well the relaxation of excitations in systems with open electron shells when the spin-orbit coupling (SOC) can be neglected and consider the α and β spin states independently. In some cases, for example, when considering *f-f* transitions in β-NaYF$_4$: Ln^{3+} (Ln = Ce, Pr) crystals (*17*) or in organic-inorganic perovskites containing heavy elements (*15*), he SOC leads to the fact that optical transitions with spin-flip become allowed, which requires further development of the theory.

The non-collinear spin (NCS) approach refers to computing on the basis of spinor orbitals. This term addresses the fact that spin vector is allowed to take any orientation, thus expectation values of magnetization vector may deviate from z-axis by having non-zero m_x and m_y components, while in regular spin-polarized DFT the magnetization vector $\vec{M} = (0,0,m_z)$. Within the noncollinear magnetism framework, the spinor KS orbitals (SKSO), ψ_i, are represented as a superposition of spin-α and spin-β states $|\alpha\rangle = \begin{bmatrix} 1 \\ 0 \end{bmatrix}$ and $|\beta\rangle = \begin{bmatrix} 0 \\ 1 \end{bmatrix}$

$$\psi_i = \varphi_i^\alpha |\alpha\rangle + \varphi_i^\beta |\beta\rangle = \begin{Bmatrix} \varphi_i^\alpha \\ \varphi_i^\beta \end{Bmatrix} \quad (37)$$

SKSOs obey the orthonormality condition:

$$\int dr \{\varphi_{i\alpha}^* \ \varphi_{i\beta}^*\} \begin{Bmatrix} \varphi_{j\alpha} \\ \varphi_{j\beta} \end{Bmatrix} = \int dr \left(\varphi_{i\alpha}^* \varphi_{j\alpha} + \varphi_{i\beta}^* \varphi_{j\beta} \right) = \delta_{ij} \quad (38)$$

where δ_{ij} is the Kronecker-delta function. The spin-orbitals are the eigenvalues of the KS equations with the Hamiltonian that includes the SOC terms, computed as

$$\widehat{H}^{Relat} = \widehat{H}^{SR} + \widehat{H}^{SOC} \quad (39)$$

where $\widehat{H}^{SR}$ and $\widehat{H}^{SOC}$ stand for scalar relativistic and spin-orbit terms, respectively. The $\widehat{H}^{SR}$ term describes relativistic kinetic energy corrections and $\widehat{H}^{SOC}$ describes energy shifts of spin occupations. The KS equations for components of a spinor orbital read

$$\sum_{\sigma'=\alpha,\beta} \left(-\delta_{\sigma\sigma'} \nabla^2 + v_{\sigma\sigma'}^{eff}(r) \right) \varphi_{i\sigma}(r) = \varepsilon_{i,\sigma\sigma'} \varphi_{i\sigma}(r) \quad (40)$$

$$v_{\sigma\sigma'}^{eff}(r) = \begin{pmatrix} v_{\alpha\alpha}^{eff}(r) & v_{\alpha\beta}^{eff}(r) \\ v_{\beta\alpha}^{eff}(r) & v_{\beta\beta}^{eff}(r) \end{pmatrix} \quad (41)$$

here σ and σ' define spin projection, $v_{\sigma\sigma'}^{eff}(r)$ is the spin-dependent external potential, and $\varphi_{i\sigma}(r)$ is a spin-dependent KS orbital. In the expression for the effective potential (41), the off-diagonal matrix elements are responsible for the mixing of spin states. When converting them to zero, we obtain formulas for the above-described case of spin-polarized states with transitions without a spin flip.

Similar to Eq. 17, the NACs can be computed using the "on-the-fly" procedure along a nuclear trajectory as

$$V_{nm} = \frac{1}{2\Delta t} \int dr \{ \varphi_{n\alpha}^*(r, R(t)), \varphi_{m\beta}^*(r, R(t)) \} \cdot$$
$$\begin{cases} \varphi_{n\alpha}(r, R(t + \Delta t)) \\ \varphi_{n\beta}(r, R(t + \Delta t)) \end{cases} + h.c. \quad (42)$$

Using the obtained expression in Eqs. (8)-(10), (18), Eq. (7) can be solved and the obtained dissipative density matrix predicts the behavior of the observables as described above in the case without taking into account the SOC. The matrix elements of the transition dipoles in the basis of two-component spinors are

$$\vec{D}_{ij} = e \int \{ \varphi_i^{\alpha*} \ \varphi_i^{\beta*} \} \vec{r} \psi_j \begin{Bmatrix} \varphi_j^\alpha \\ \varphi_j^\beta \end{Bmatrix} dr = \int \left(\varphi_i^{\alpha*}(r) \ r \ \varphi_j^\alpha(r) + \right.$$
$$\left. \varphi_i^{\beta*}(r) \ r \ \varphi_j^\beta(r) \right) dr \quad (43)$$

Further, we apply the developed approach to investigate the roles of surface passivation and doping on the non-equilibrium charge relaxation in cesium lead perovskite ($CsPbI_3$) nanocrystals (NC) (15).

In NCS DFT the magnetization vector $\vec{M} = (M_x, M_y, M_z)$ is constructed from the magnetization densities $m_i(r)$ as $M_i = \int dr \, m_i(r), \ i = x, y, z$. Total charge density and $m_i(r)$ are found from SKSO density matrix $\hat{\rho}^{NCS}(r) = \begin{pmatrix} \hat{\rho}_{\alpha\alpha}(r) & \hat{\rho}_{\alpha\beta}(r) \\ \hat{\rho}_{\beta\alpha}(r) & \hat{\rho}_{\beta\beta}(r) \end{pmatrix}$. Components within the density matrix are found from $\hat{\rho}_{\sigma\sigma'}(r) = \sum_i f_i^{NCS} \varphi_{i\sigma}(r) \ \varphi_{i\sigma'}(r)$. f_i^{NCS} is the occupation number of the ith SKSO and takes values between 0 and 1.

$$\rho(r) = \rho_{\alpha\alpha}(r) + \rho_{\beta\beta}(r) \quad (44)$$

$$m_i(r) = \mu_B Tr(\hat{\rho}^{NCS}(r)\hat{\sigma}_i) \quad (45)$$

where μ_B and $\hat{\sigma}_i$ are Bohr magneton and Pauli matrices, respectively.

The presented theoretical method allows calculating the evolution of the electronic structure of the objects under study. Using Eqs (24) and (45), it is possible to analyze the dynamics of filling of electron orbitals and the distribution of spin density in the systems under study. The former value corresponds to the change in the degree of oxidation of atoms during relaxation and electronic excitations; the latter one is responsible for the evolution of the spin distribution. In the case of a sufficiently strong spin-orbit interaction, a change in the multiplicity of heavy ions is possible, which can also be quantitatively described.

Example: Charge Dynamics in Pristine and Mn-Doped CsPbI$_3$ Nanocrystals

We use spinor Kohn-Sham orbitals (SKSOs) with spin-orbit coupling (SOC) interaction as a basis to compute excited-state dissipative dynamics simulations on a fully-passivated CsPbBr$_3$

nanocrystal (NC) atomistic model. Fully inorganic lead halide perovskite $CsPbBr_3$ NCs are of interest for optoelectronic and light-emitting devices because of their photoluminescence emission properties, which can be tuned/optimized by surface passivation and doping. SOC is important in $CsPbI_3$ because it contains heavy elements Pb and I. To describe the influence of SOCs on the electronic properties and relaxation processes of excitations, the NCs under study were considered in the spin-polarized and spinor basis sets.
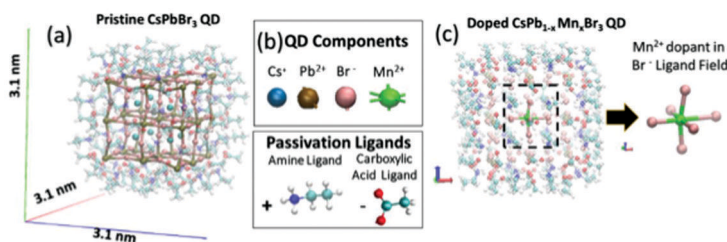

Figure 4. (a) Geometry-optimized pristine CsPbBr 3 NC constructed from a 2 × 2 × 2 unit cell and passivated by short-chain carboxylic acid and amine ligands. The pristine NC has an atomistic composition of $Cs_8Pb_{27}Br_{54}$ + 48 ethylammonium cations + 54 acetate anions. (b) Elements/molecules used to construct the perovskite NC models. (c) Mn 2+ -doped $CsPb_{1-x}Mn_xBr_3$ NC which has the same morphology as the intrinsic NC but with the central most Pb^{2+} atom substitutionally replaced with Mn^{2+}. Reproduced with permission from reference (13). Copyright 2016 American Chemical Society.

Construction of the fully-passivated $CsPbBr_3$ atomistic model follows experimental observations regarding surface termination. It is observed that with decreased $CsPbBr_3$ edge length the stoichiometry of Pb^{2+} and Br^- increase relative to Cs^+, providing a 'Pb-rich' surface (60). This indicates that smaller NCs take on a Pb-Br surface termination which requires a deprotonated oleic acid to bind to surface Pb^{2+} and oleylammonium to coordinate to surface Br^-. Thus we took the bulk $CsPbBr_3$ crystal structure, carved out a 2x2x2 unit cell, and coordinated acetate/ethylammonium ions to surface atoms Pb^{2+}/Br^-. Overall, this gives a structure of $Cs_8Pb_{27}Br_{54}$ passivated with 54/48 acetate/ethylammonium ligands for a total of 995 atoms as it is shown in Figure 4. This composition gives a NC that has an edge length of ~1.5 nm. For the doped NC, the Mn^{2+} ion substitutionally replaces the central most Pb^{2+} atom giving an atomistic configuration of $Cs_8Pb_{26}MnBr_{54}$ with the same surface passivation configuration as the pristine NC.

Optical properties of considered NCs were computed using Eqs (32),(33),(43) for both intrinsic and doped NCs under different bases and are shown in Figure 5 with numerical details of the brightest transitions presented in Table 3. Labels a−c indicate spin-conserving transitions and *d-f* indicate spin-flip transitions with alphabetic progression of labels guiding from UV to IR ranges. Table 3 shows the greatest contributing transition for each of the labeled peaks in Figure 5. Calculations taking into account the SOC leads to the above narrowing of the width of the optical gap in comparison with the results obtained without considering it.
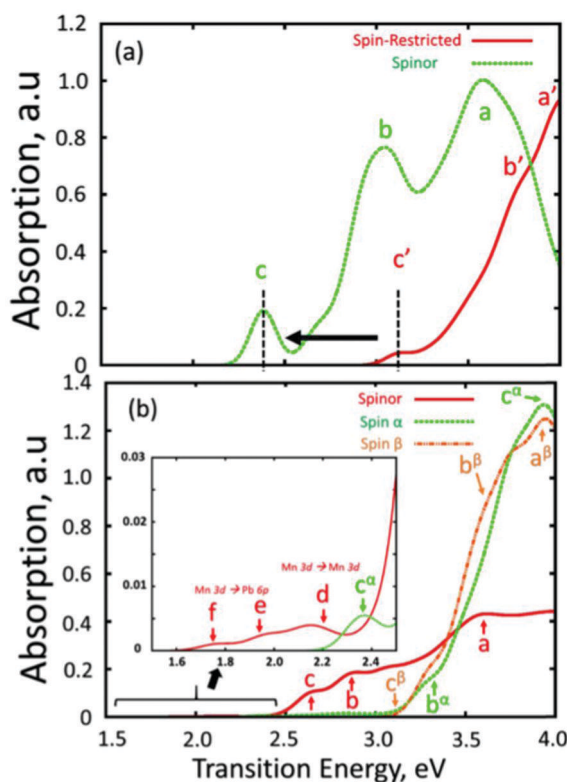
Figure 5. Optical spectra (in arbitrary units) for fully-passivated (a) pristine CsPbBr₃ NC and (b) doped CsPb₁₋ₓMnₓBr₃ NC. Labels indicating notable optical transitions are described in Table 3. (a) Solid red line corresponds to KS spectra and the dashed green line corresponds to spinor spectra. The spinor spectra show lower transition energies because of SOC reducing the band gap. Spinor spectra also show enhanced onset absorption compared to SR spectra (vertical black dashed lines). (b) Solid red, dashed green, and dashed-hyphen orange lines correspond to spinor, spin-α, and spin-β spectra, respectively. The inset shows low-intensity absorption onset for spinor and spin-α spectra. The spinor spectra show earlier onset of absorption compared to spin-polarized KS spectra. Reproduced with permission from reference (13). Copyright 2016 American Chemical Society.

The resulting bright optical transitions were used as initial states to consider the relaxation of the corresponding excitations. The values of Redfield tensor, which depend on NACs, are visualized in Figure 6 and have values in the range of 10^{-4} to 50 ps^{-1}. Redfield tensors for both pristine and doped NCs are shown in Figure 6, respectively. KSO indices i and j are plotted on x-axis and y-axis with matrix elements R_{iijj} plotted on the z-axis. For the pristine NC, Figure 6a corresponds to Redfield tensor elements computed using the SR KSO basis and Figure 6b corresponds to the SKSO basis. SR KSO and SKSO tensor elements show drastically different trends. For the SR KSO basis, numerical values of tensor elements decrease as they approach the band edge and decrease

$$R_{ii,jj} \approx \begin{cases} R_0 |\varepsilon_i - \varepsilon_{LU}| \delta_{i,j+1}, i \geq j \\ R_0 |\varepsilon_{HO} - \varepsilon_i| \delta_{i,j+1}, i \leq j \end{cases}$$

continuously closer to the band edge, in accordance with the gap law (61). The SKSO electronic structure produced twofold degenerate energy states. In this basis, R_{iijj} elements show a discontinuous stepwise change $R_{ii,jj} \approx R_0 \delta_{i,j+1} \frac{1+(-1)^2}{2}$, where last

factor alternates between zero and one. The fast $R_{\text{ii},i-1,i-1}$ transitions occur between degenerate states $E_{\text{SKSO}}(i) = E_{\text{SKSO}}(i-1)$ and slower rates between nondegenerate states $E_{\text{SKSO}}(i) \neq E_{\text{SKSO}}(i-1)$. Therefore, the tensor elements $R_{\text{ii},i-n,i-n}$ contribute toward relaxation when $n > 1$. Even with lower absolute rates of relaxation for the SKSO basis, compared to the SR basis, nonradiative relaxation to band edges is slightly quicker in the SKSO basis. This can be attributed to the SKSO basis mixing with a larger number of states which provide a greater number of nonradiative relaxation pathways, that is, the SKSO Redfield tensor has more off-diagonal elements compared to the KS tensor.

Table 3. Optical transitions for pristine and doped NCs using different bases (Figure 5)

	Pristine, KS					Pristine, SKSO			
	i	j	E_{ij}, eV	OS		i	j	E_{ij}, eV	OS
c'	HO	LU	3.11	6.73	c	HO	LU	2.38	0.22
b'	HO-3	LU+16	3.72	4.52	b	HO-6	LU+11	3.18	0.47
a'	HO-37	LU+2	4.01	2.61	a	LU+29	HO-28	3.69	0.15
	Mn-doped, KSO, spin α					Mn-doped, KSO, spin β			
c^{α}	HO	LU	2.37	0.47	c^{β}	HO	LU	3.13	0.08
b^{α}	HO-3	LU+1	3.27	3.70	b^{β}	HO-7	LU+8	3.62	5.20
a^{α}	HO-20	LU+9	7.12	7.12	a^{β}	HO-17	LU+14	3.98	1.76
	Mn-doped, SKSO								
	i	j	E_{ij}, eV	OS		i	j	E_{ij}, eV	OS
f	HO	LU	1.76	0.02	c	HO-5	LU+1	2.63	0.46
e	HO	LU+4	1.91	0.01	b	HO-7	LU+4	2.80	0.46
d	HO	LU+12	2.20	0.01	a	HO-31	LU+29	3.62	0.08

For the doped NC, it was observed that the hole relaxation rate is 10^2 faster in the spin-α basis than in the SKSO basis. This is interesting as the spin-α and SKSO valence bands are basically identical in atomic orbital composition and in energy differences between states. Non-adiabatic transitions are generally inversely proportional to the energy difference between states and proportional to the mixing of states. Because the energetics are the same between the two bases, the difference must be a result of difference in "spin mixing". The difference between the spin-α and SKSO relaxation is in the HO-2→HO-1 and HO-1→HO transitions. A population "bottleneck" appears in the SKSO basis compared to spin-α. We attribute the "bottleneck" to two factors: (1) HO-2 to HO-1, or HO, is a low probability spin-flip transition, which is not considered in the spin-α basis. (2) The HO-1 and HO transition is a transition between Br-4p-hybridized Mn^{2+} 3d states. Contributions from mixing between Mn^{2+} $3d_{x^2-y^2}$ and $3d_{z^2}$ will be a negligible contribution to nonradiative relaxation, so the relaxation between HO-1 and HO is driven by the hybridized Br-4p. Note that in the NCS approach, the direction of spin magnetization may deviate from the conventionally used z-axis.
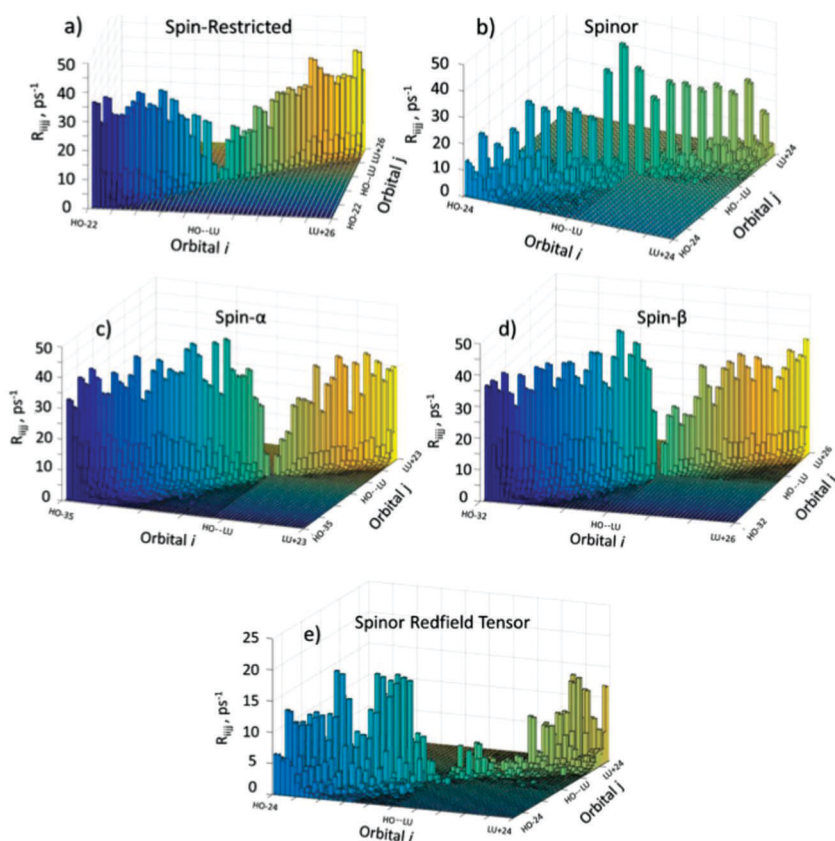
Figure 6. Redfield tensors computed for the fully passivated (a−b) pristine CsPbBr$_3$ NC and (c−e) doped CsPb$_{1-x}$Mn$_x$Br$_3$ NC. Redfield tensors describe the average coupling of electronic states i (x-axis) and j (y-axis) along a MD trajectory because of thermal fluctuations. Each R$_{iijj}$ component (z-axis) is proportional to the rate of transition between states i and j. For the pristine NC, (a) shows greater coupling away from the band edge and lower coupling near the band edge, whereas (b) shows the opposite trend. Reproduced with permission from reference (13). Copyright 2016 American Chemical Society.

Conclusion

We introduced the methodology for theoretical description of nonadiabatic charge dynamics in spin-polarized semiconducting systems. In the simplest case, when SOC can be neglected, electron states with α- and β projections of the spin onto the quantization axis can be considered independently. When considering systems with open shells, it is natural to expect that relaxation of electrons with α- and β will occur differently. This has been confirmed by numerical data in the case of vanadium doped TiO$_2$, with doublet ground state configuration. It is shown that several classes of pathways, selected by excitation and spin polarization of α- and β-transitions, have completely different relaxation dynamics even with similar transition energies. A photon of a given wavelength can therefore induce two independent and noncoinciding pathways of photoinduced dynamics.

A natural extension of this approach is incorporation of SOC into excited-state nonadiabatic dynamics simulations using density matrix formalism to describe radiative and nonradiative relaxation processes. NACs between nuclear and electronic degrees of freedom were computed in the basis of SKSOs found from NCS DFT. We apply this method to a pristine CsPbBr$_3$ and a Mn^{2+}-

doped $CsPb_{1-x}Mn_xBr_3$ perovskite NC to reveal how spin-orbit interaction influences ground-state electronic/optical properties and excited-state electron dynamics. A new approach demonstrates NACs computed with SKSOs for the pristine NC provided different trends in non-radiative relaxation rates. Our results demonstrate that taking into account of SOC is critical in the study of intraband relaxation.

References

1. Chen, X.; Shen, S.; Guo, L.; Mao, S. Semiconductor-Based Photocatalytic Hydrogen Generation. *Chem. Rev.* **2010**, *110*, 6503–6570.

2. Kärkäs, M. D.; Verho, O.; Johnston, E. V.; Åkermark, B. Artificial Photosynthesis: Molecular Systems for Catalytic Water Oxidation. *Chem. Rev.* **2014**, *114*, 11863–12001.

3. Wisser, M.; Fischer, S.; Maurer, P.; Bronstein, N.; Chu, S.; Alivisatos, A.; Salleo, A.; Dionne, J. Enhancing Quantum Yield Via Local Symmetry Distortion in Lanthanide-Based Upconverting Nanoparticles. *ACS Photonics* **2016**, *3*, 1523–1530.

4. Zhang, Y.; Wang, Y.; Song, J.; Qu, J.; Li, B.; Zhu, W.; Wong, W. Near-Infrared Emitting Materials Via Harvesting Triplet Excitons: Molecular Design, Properties, and Application in Organic Light Emitting Diodes. *Adv. Opt. Mater.* **2018**, *6*, 1800466.

5. Asbury, J. B.; Hao, E.; Wang, Y.; Ghosh, H. N.; Lian, T. Ultrafast Electron Transfer Dynamics from Molecular Adsorbates to Semiconductor Nanocrystalline Thin Films. *J. Phys. Chem. B* **2001**, *105*, 4545–4557.

6. Petek, H.; Zhao, J. Ultrafast Interfacial Proton-Coupled Electron Transfer. *Chem. Rev.* **2010**, *110*, 7082–7099.

7. Duncan, W.; Prezhdo, O. Theoretical Studies of Photoinduced Electron Transfer in Dye-Sensitized TiO_2. *Annu. Rev. Phys. Chem.* **2007**, *58*, 143–184.

8. Hilgendorff, M.; Sundström, V. Dynamics of Electron Injection and Recombination of Dye-Sensitized TiO_2 Particles. *J. Phys. Chem. B* **1998**, *102*, 10505–10514.

9. Kudo, A.; Miseki, Y. Heterogeneous Photocatalyst Materials for Water Splitting. *Chem. Soc. Rev.* **2009**, *38*, 253–278.

10. Brenner, T.; Egger, D.; Kronik, L.; Hodes, G.; Cahen, D. Hybrid Organic-Inorganic Perovskites: Low-Cost Semiconductors with Intriguing Charge-Transport Properties. *Nat. Rev. Mater.* **2016**, *1*, 15007.

11. Wen, S.; Zhou, J.; Zheng, K.; Bednarkiewicz, A.; Liu, X.; Jin, D. Advances in Highly Doped Upconversion Nanoparticles. *Nat. Commun.* **2018**, *9*, 2415.

12. *Silicon and Silicide Nanowires Applications, Fabrication, and Properties*; Pan Stanford Publishing: Singapore, 2014.

13. Li, W.; Zhou, L.; Prezhdo, O.; Akimov, A. Spin–Orbit Interactions Greatly Accelerate Nonradiative Dynamics in Lead Halide Perovskites. *ACS Energy Lett.* **2018**, *3*, 2159–2166.

14. Vogel, D.; Kryjevski, A.; Inerbaev, T.; Kilin, D. Photoinduced Single- and Multiple-Electron Dynamics Processes Enhanced by Quantum Confinement in Lead Halide Perovskite Quantum Dots. *J. Phys. Chem. Lett.* **2017**, *8*, 3032–3039.

15. Forde, A.; Inerbaev, T.; Kilin, D. Spinor Dynamics in Pristine and Mn^{2+}-Doped $CsPbBr_3$ NC: Role of Spin–Orbit Coupling in Ground- and Excited-State Dynamics. *J. Phys. Chem. C* **2018**, *122*, 26196–26213.

16. Forde, A.; Inerbaev, T.; Hobbie, E.; Kilin, D. Excited-State Dynamics of a $CsPbBr_3$ Nanocrystal Terminated with Binary Ligands: Sparse Density of States with Giant Spin–Orbit Coupling Suppresses Carrier Cooling. *J. Am. Chem. Soc.* **2019**, *141*, 4388–4397.

17. Han, Y.; Vogel, D. J.; Inerbaev, T. M.; May, P.; Berry, M.; Kilin, D. Photoinduced Dynamics to Photoluminescence in Ln^{3+} (Ln = Ce, Pr) Doped B-$NaYF_4$ Nanocrystals Computed in Basis of Non-Collinear Spin Dft with Spin-Orbit Coupling. *Mol. Phys.* **2018**, *116*, 697–707.

18. Nitzan, A. *Chemical Dynamics in Condensed Phases: Relaxation, Transfer, and Reactions in Condensed Molecular Systems*; Oxford University Press: USA, 2006.

19. Tully, J. Molecular Dynamics with Electronic Transitions. *J. Chem. Phys.* **1990**, *93*, 1061–1071.

20. Pechukas, P. Time-Dependent Semiclassical Scattering Theory. I. Potential Scattering. *Phys. Rev.* **1969**, *181*, 166–174.

21. Pradhan, E.; Sato, K.; Akimov, A. Non-Adiabatic Molecular Dynamics with ΔSCF Excited States. *J. Phys.: Condens. Matter* **2018**, *30*, 484002.

22. Miller, W. The Semiclassical Initial Value Representation: A Potentially Practical Way for Adding Quantum Effects to Classical Molecular Dynamics Simulations. *J. Phys. Chem. A* **2001**, *105*, 2942–2955.

23. Shi, Q.; Geva, E. A Semiclassical Generalized Quantum Master Equation for an Arbitrary System-Bath Coupling. *J. Chem. Phys.* **2004**, *120*, 10647–10658.

24. Poulsen, J.; Nyman, G.; Rossky, P. Practical Evaluation of Condensed Phase Quantum Correlation Functions: A Feynman–Kleinert Variational Linearized Path Integral Method. *J. Chem. Phys.* **2003**, *119*, 12179–12193.

25. Meyera, H.; Miller, W. A Classical Analog for Electronic Degrees of Freedom in Nonadiabatic Collision Processes. *J. Chem. Phys.* **1979**, *70*, 3214–3223.

26. Stock, G.; Thoss, M. Semiclassical Description of Nonadiabatic Quantum Dynamics. *Phys. Rev. Lett.* **1997**, *78*, 578–581.

27. Redfield, A. On the Theory of Relaxation Processes. *IBM J. Res. Dev.* **1957**, *1*, 19–31.

28. Leggett, A.; Chakravarty, S.; Dorsey, A.; Fisher, M.; Garg, A.; Zwerger, W. Dynamics of the Dissipative Two-State System. *Rev. Mod. Phys.* **1987**, *59*, 1–85.

29. Th, F. Transfer Mechanisms of Electronic Excitation Energy. *Radiat. Res. Suppl.* **1960**, *2*, 326–339.

30. De Angelis, F.; Di Valentin, C.; Fantacci, S.; Vittadini, A.; Selloni, A. Theoretical Studies on Anatase and Less Common Tio2 Phases: Bulk, Surfaces, and Nanomaterials. *Chem. Rev.* **2014**, *114*, 9708–9753.

31. Yao, G.; Berry, M.; May, P.; Kilin, D. DFT Calculation of Russell-Saunders Splitting for Lanthanide Ions Doped in Hexagonal (Beta)-Nayf4 Nanocrystals. *J. Phys. Chem. C* **2013**, *117*, 17177–17185.

32. Parr, R. G.; Yang, W. *Density-Functional Theory of Atoms and Molecules*; Oxford University Press: New York, Oxford, 1989.

33. Jensen, S.; Inerbaev, T.; Kilin, D. Spin Unrestricted Excited State Relaxation Study of Vanadium(IV)-Doped Anatase. *J. Phys. Chem. C* **2016**, *120*, 5890–5905.

34. Egorova, D.; Thoss, M.; Domcke, W.; Wang, H. Modeling of Ultrafast Electron-Transfer Processes: Validity of Multilevel Redfield Theory. *J. Chem. Phys.* **2003**, *119*, 2761–2773.

20

Kilin et al.; Computational Photocatalysis: Modeling of Photophysics and Photochemistry at Interfaces
ACS Symposium Series; American Chemical Society: Washington, DC, 2019.

35. Pollard, W.; Friesner, R. Solution of the Redfield Equation for the Dissipative Quantum Dynamics of Multilevel Systems. *J. Chem. Phys.* **1994**, *100*, 5054–5065.

36. Jean, J.; Friesner, R.; Fleming, G. Application of a Multilevel Redfield Theory to Electron Transfer in Condensed Phases. *J. Chem. Phys.* **1992**, *96*, 5827–5842.

37. Sundström, V.; Pullerits, T.; van Grondelle, R. Photosynthetic Light-Harvesting: Reconciling Dynamics and Structure of Purple Bacterial Lh2 Reveals Function of Photosynthetic Unit. *J. Phys. Chem. B* **1999**, *103*, 2327–2346.

38. Kühn, O.; May, V.; Schreiber, M. Dissipative Vibrational Dynamics in a Curve–Crossing System. *J. Chem. Phys.* **1994**, *101*, 10404–10415.

39. Venkataraman, C.; Soudackov, A.; Hammes-Schiffer, S. Dynamics of Photoinduced Proton-Coupled Electron Transfer at Molecule−Semiconductor Interfaces: A Reduced Density Matrix Approach. *J. Phys. Chem. C* **2010**, *114*, 487–496.

40. Baiz, C.; Kubarych, K.; Geva, E. Molecular Theory and Simulation of Coherence Transfer in Metal Carbonyls and Its Signature on Multidimensional Infrared Spectra. *J. Phys. Chem. B* **2011**, *115*, 5322–5339.

41. Hammes-Schiffer, S.; Tully, J. Proton Transfer in Solution: Molecular Dynamics with Quantum Transitions. *J. Chem. Phys.* **1994**, *101*, 4657–4667.

42. Kilina, S.; Craig, C.; Kilin, D.; Prezhdo, O. Ab Initio Time-Domain Study of Phonon-Assisted Relaxation of Charge Carriers in a Pbse Quantum Dot. *J. Phys. Chem. C* **2007**, *111*, 4871–4878.

43. Kilin, D.; Micha, D. Relaxation of Photoexcited Electrons at a Nanostructured Si(111) Surface. *J. Phys. Chem. Lett.* **2010**, *1*, 1073–1077.

44. Nelson, T.; Fernandez-Alberti, S.; Roitberg, A.; Tretiak, S. Nonadiabatic Excited-State Molecular Dynamics: Modeling Photophysics in Organic Conjugated Materials. *Acc. Chem. Res.* **2014**, *47*, 1155–1164.

45. Kohn, W.; Sham, L. Self-Consistent Equations Including Exchange and Correlation Effects. *Phys. Rev.* **1965**, *140*, 1133–1138.

46. Parr, R.; Yang, W. , *Density-Functional Theory of Atoms and Molecules*; Oxford University Press, 1994.

47. Kresse, G.; Furthmüller, J. Efficiency of Ab-Initio Total Energy Calculations for Metals and Semiconductors Using a Plane-Wave Basis Set. *Comput. Mater. Sci.* **1996**, *6*, 15–50.

48. Kresse, G.; Furthmüller, J. Efficient Iterative Schemes for Ab Initio Total-Energy Calculations Using a Plane-Wave Basis Set. *Phys. Rev. B* **1996**, *54*, 11169–11186.

49. Blochl, P. Projector Augmented-Wave Method. *Phys. Rev. B* **1994**, *50*, 17953–17979.

50. Kresse, G.; Joubert, D. From Ultrasoft Pseudopotentials to the Projector Augmented-Wave Method. *Phys. Rev. B* **1999**, *59*, 1758–1775.

51. Perdew, J.; Burke, K.; Ernzerhof, M. Generalized Gradient Approximation Made Simple. *Phys. Rev. Lett.* **1996**, *77*, 3865–3868.

52. Englman, R.; Jortner, J. Energy Gap Law for Radiationless Transitions in Large Molecules. *Mol. Phys.* **1970**, *18*, 145–164.

53. Kalantari, K.; Kalbasi, M.; Sohrabi, M.; Royaeee, S. Enhancing the Photocatalytic Oxidation of Dibenzothiophene Using Visible Light Responsive Fe and N Co-Doped TiO_2 Nanoparticles. *Ceram. Int.* **2017**, *43*, 973–981.

54. Martin, S.; Morrison, C.; Hoffmann, M. Photochemical Mechanism of Size-Quantized Vanadium-Doped TiO$_2$ Particles. *J. Phys. Chem.* **1994**, *98*, 13695–13704.

55. Wachs, I.; Saleh, R.; Chan, S.; Chersich, C. The Interaction of Vanadium Pentoxide with Titania (Anatase): Part I. Effect on O-Xylene Oxidation to Phthalic Anhydride. *Appl. Catal.* **1985**, *15*, 339–352.

56. Saleh, R.; Wachs, I.; Chan, S.; Chersich, C. The Interaction of V$_2$O$_5$ with TiO$_2$ (Anatase): Catalyst Evolution with Calcination Temperature and O-Xylene Oxidation. *J. Catal.* **1986**, *98*, 102–114.

57. Machej, T.; Haber, J.; Turek, A.; Wachs, I. Monolayer V$_2$O$_5$/TiO$_2$ and MoO$_3$/TiO$_2$ Catalysts Prepared by Different Methods. *Appl. Catal.* **1991**, *70*, 115–128.

58. Deo, G.; Turek, A.; Wachs, I.; Machej, T.; Haber, J.; Das, N.; Eckert, H.; Hirt, A. Physical and Chemical Characterization of Surface Vanadium Oxide Supported on Titania: Influence of the Titania Phase (Anatase, Rutile, Brookite and B). *Appl. Catal. A: Gen.* **1992**, *91*, 27–42.

59. Laporte, O.; Meggers, W. Some Rules of Spectral Structure. *J. Opt. Soc. Am.* **1925**, *11*, 459–463.

60. Maes, J.; Balcaen, L.; Drijvers, E.; Zhao, Q.; De Roo, J.; Vantomme, A.; Vanhaecke, F.; Geiregat, P.; Hens, Z. Light Absorption Coefficient of CsPbBr$_3$ Perovskite Nanocrystals. *J. Phys. Chem. Lett.* **2018**, *9*, 3093–3097.

61. Englman, R.; Jortner, J. The Energy Gap Law for Radiationless Transitions in Large Molecules. *Mol. Phys.* **1970**, *18*, 145–164.

22

Kilin et al.; Computational Photocatalysis: Modeling of Photophysics and Photochemistry at Interfaces
ACS Symposium Series; American Chemical Society: Washington, DC, 2019.